Materials Science & Engineering A 746 (2019) 82–93

Contents lists available at ScienceDirect

Materials Science & Engineering A

journal homepage: www.elsevier.com/locate/msea

Effects of Zn and Ca addition on microstructure and mechanical properties of as-extruded Mg-1.0Sn alloy sheet

Yanfu Chai[a], Bin Jiang[a,b,*], Jiangfeng Song[a], Bo Liu[c], Guangsheng Huang[a], Dingfei Zhang[a], Fusheng Pan[a,b]

[a] State Key Laboratory of Mechanical Transmissions, College of Materials Science and Engineering, Chongqing University, Chongqing 400044, China
[b] Chongqing Academy of Science and Technology, Chongqing 401123, China
[c] Chongqing Chang-an Automobile Co., Ltd., Chongqing 400023, China

ARTICLE INFO

Keywords:
Mg-1.0Sn alloy
Zn and Ca content
Microstructure
Strain hardening behaviour
Mechanical properties

ABSTRACT

The microstructure and mechanical properties of as-extruded Mg-1.0Sn, Mg-1.0Sn-0.5Zn, Mg-1.0Sn-0.7Ca and Mg-1.0Sn-0.5Zn-0.5Ca (all in wt%) alloy sheets were investigated and compared at room temperature. The results showed that the Mg-1.0Sn and Mg-1.0Sn-0.5Zn alloys exhibited relatively coarse grains and typical strong basal textures, whereas the Mg-1.0Sn-0.7Ca and Mg-1.0Sn-0.5Zn-0.5Ca alloys showed obvious grain refinement and weakened extrusion direction (ED)-split textures. The yield strength and ductility of the Mg-1.0Sn-0.5Zn alloy increased by approximately 20 MPa and 5%, respectively, than that of the Mg-1.0Sn alloy. Despite the similar ductilities of the Mg-1.0Sn-0.5Zn and Mg-1.0Sn-0.7Ca alloys, the yield strength improvement was more remarkable in the Mg-1.0Sn-0.7Ca alloy. In particular, the yield strength of the Mg-1.0Sn-0.7Ca alloy in tension along transverse direction was 209 MPa, which was about 73 MPa higher than that of the Mg-1.0Sn alloy. This was attributed mainly to the grain refinement from ~26 μm to ~9 μm and the precipitation strengthening induced by homogeneous distributed, spherical Mg_2Ca nano-particles. Furthermore, ductility of the Mg-1.0Sn-0.5Zn-0.5Ca alloy in tension along the ED could reach up to 30.5%, which was almost twice that of the Mg-1.0Sn-0.7Ca alloy, because of increased activation of prismatic slip, enhanced grain boundary cohesion and improved intergranular strain propagation capacity. Therefore, individual addition of dilute Zn or Ca contributed to an improvement in the strength and ductility of the Mg-1.0Sn alloy, whereas combined addition of dilute Zn and Ca provided a new approach for achieving excellent ductility of the Mg-1.0Sn alloy.

1. Introduction

Owing to the low density, high specific strength and specific stiffness, and satisfactory damping capacity of Mg alloys, they have attracted worldwide attention, particularly in the aerospace, automobile, missile, and 3 C industries [1–3]. However, unsatisfactory strength and ductility of these alloys severely limit their further applications. Generally, addition of alloy elements, especially rare-earth (RE) elements, has been recognized as an effective and practical method to improve the mechanical properties of Mg alloys [4–7]. Unfortunately, RE elements are expensive and have adverse effects on the environment when utilized [8]. In recent years, Sn, which is a low-cost element, has attracted more attention than RE elements for alloying with Mg. Liu et al. [9] reported that the addition of 5 wt% Sn to pure Mg resulted in increments of about 40.7% and 39.9% in the ultimate tensile strength (UTS) and elongation to failure (EL), respectively. Zhao et al. [10] also found that the yield strength, UTS and EL of as-extruded Mg bars increased with an increase in the Sn content from 1.3 wt% to 4.7 wt%. The reason for this increase was that Sn addition induced changes in the grain size, secondary phase, and distribution of grain orientation. Furthermore, Sn addition was also reported to decrease the unstable stacking fault energy and lead to the activation of slip systems [11]. Therefore, the Mg-Sn alloy system was a promising candidate for the development of high-performance Mg alloys [12–14].

Recently, a system of high-strength Mg-Sn-based alloys was developed, whose high strength could be predominately ascribed to the high Sn content and subsequent aging treatment [15,16]. As is well known, the solubility of the Sn element in α-Mg is strongly dependent on temperature. It decreases sharply from 14.85 wt% at 561 °C to just 0.45 wt% at 200 °C, this temperature dependence is the basis for the

* Corresponding author at: State Key Laboratory of Mechanical Transmissions, College of Materials Science and Engineering, Chongqing University, Chongqing 400044, China.
E-mail address: jiangbinrong@cqu.edu.cn (B. Jiang).

https://doi.org/10.1016/j.msea.2019.01.028
Received 27 May 2018; Received in revised form 5 January 2019; Accepted 7 January 2019
Available online 08 January 2019
0921-5093/

strength improvement of Mg-Sn-based alloys via precipitation hardening. Unfortunately, a high Sn content would inevitably increase the costs, and Mg-Sn binary alloys still exhibit sluggish ageing kinetics and low ductility [17]. Hence, with the aim of lowering the cost of Mg-Sn-based alloy systems and improving their mechanical properties, recent studies have been focused on micro-alloyed systems with low Sn content [12,18]. Zn and Ca elements have received increasing attention in recent years because they are inexpensive and commonly available. Sasaki et al. [19] reported that the addition of 0.5 at% Zn substantially increased the peak hardness of Mg-2.2Sn alloy. Pan et al. [20] found that an indirect-extruded Mg-2Sn-2Ca (wt%) alloy possessed an ultra-high tensile yield strength (360–440 MPa). Moreover, they also developed a new wrought Mg-2Sn-1Ca-2Zn (wt%) alloy with a yield strength of 218 MPa and an elongation of 23% [21]. Previous studies on Mg-Zn-Ca ternary alloys [22–24] have shown that minor additions (0–1.0 wt %) of Zn and Ca elements have a strong influence on the mechanical properties of Mg alloys, especially on their ductile performance. However, thus far, the effects of individual additions of dilute Zn and Ca and their combined addition on the microstructure, texture, and mechanical properties of Mg-Sn-based alloys with low Sn content have rarely been studied. Furthermore, a systematic comparison of the strain hardening behaviour of Mg-Sn alloy with those of Mg-Sn-Zn, Mg-Sn-Ca, and Mg-Sn-Zn-Ca alloys under uniaxial tensile loading remains to be performed. Consequently, in the present work, the microstructure, texture, mechanical properties, and strain hardening behaviours of four as-extruded alloys Mg-1.0Sn, Mg-1.0Sn-0.5Zn, Mg-1.0Sn-0.7Ca, and Mg-1.0Sn-0.5Zn-0.5Ca (all in wt%) were primarily investigated and compared.

2. Experimental procedure

Commercially pure Mg (99.8 wt%), pure Sn (99.8 wt%), pure Zn (99.8 wt%), and Mg-20 Ca (wt%) master alloys were used to prepare ingots of Mg-1.0Sn (alloy I), Mg-1.0Sn-0.5Zn (alloy II), Mg-1.0Sn-0.7Ca (alloy III), and Mg-1.0Sn-0.5Zn-0.5Ca (alloy IV) (all in wt%). Fusion metallurgy was performed in an electrical resistance furnace at 720 °C under a CO_2 + 0.5 vol% SF_6 protective gas environment. The melt was agitated for 10 min, held at 680 °C for 20 min, and then cast into a cylindrical steel mould (Φ85 mm) preheated to 300 °C. The actual chemical compositions of the experimental alloys were inspected by X-ray fluorescence spectrometry (XRF-1800CCDE), and the relevant results were presented in Table 1. Subsequently, the as-cast ingots were milled to cylindrical samples (Φ80 mm × 100 mm) and then homogenised at 400 °C for 12 h for subsequent extrusion. The extrusion process was conducted at 400 °C with ram speed of 1 mm s^{-1} and extrusion ratio of 32 to obtain a sheet with 56 mm in width and 3 mm in thickness. Uniaxial tensile tests were conducted on a CMT6305-300kN universal testing machine at a constant speed of 1 mm/min with a gauge length of 10 mm and cross-sectional areas of 6 mm × 3 mm. Three samples were tested under each condition, and the resulting data were averaged.

Phase identification was performed by X-ray diffraction (XRD; D/Max-2500/PC). The micro-structures of the as-extruded alloys were characterised by scanning electron microscopy (SEM; Tescan Vega 3 LMH) combined with energy-dispersive X-ray spectroscopy (EDS). Samples for SEM observations were ground, polished, and then etched with a mixture solution of 100 ml ethanol, 10 ml water, 5 ml acetic acid, and 5 g picric acid. The volume fraction of secondary-phase particles was evaluated using Image-Pro Plus software, and the final values were determined by averaging the values obtained from at least fifteen separate SEM images. To further reveal the precipitated phase particles formed in alloys III and IV, transmission electron microscopy (TEM; Tecnai G2 F20 S-TWIN) was also adopted with an accelerating voltage of 200 kV. Thin foil specimens for TEM observation were prepared through mechanical polishing and ion-beam thinning using a Gatan Precision Ion Polishing System at room temperature. Samples for electron backscatter diffraction (EBSD) analysis were prepared by metallurgical polishing and subsequent electro-polishing in an AC2 electrolyte through application of a voltage of 20 V for ~70 s at −20 °C. EBSD data were acquired using a JEOL JSM-7800F scanning electron microscope operating at 20 kV with a step size of 0.5 μm and then analysed with orientation imaging microscopy (OIM, HKL-channel 5) software. Besides, to better understand the deformation mechanisms of as-extruded sheets during the tensile test, in-grain misorientation axes analysis (IGMA) was employed. The misorientation angle included in this analysis was selected between 0.5 and 2.0 deg. Deformation mechanisms in deformed grains were examined by considering the dominant misorientation axis. The misorientation axes were based on all possible neighbouring measurement-point pairs belonging to the grain, and by contouring the density on the standard unit triangle.

Table 1
Chemical compositions of Mg-1.0Sn-based alloys.

Name	Nominal alloy	Composition (wt%)			
		Sn	Zn	Ca	Mg
Alloy I	Mg-1.0Sn	1.07	–	–	Bal.
Alloy II	Mg-1.0Sn-0.5Zn	1.16	0.48	–	Bal.
Alloy III	Mg-1.0Sn-0.7Ca	1.28	–	0.69	Bal.
Alloy IV	Mg-1.0Sn-0.5Zn-0.5Ca	1.10	0.55	0.47	Bal.

3. Results

3.1. Microstructure characterization

The microstructures and secondary phases of the four alloys are visualised and characterised by using backscattered electron (BSE) SEM micrographs (Fig. 1) and XRD patterns (Fig. 2), respectively. As shown in Fig. 1, few precipitates are present in the Mg-1.0Sn and Mg-1.0Sn-0.5Zn alloys (i.e. alloys I and II, respectively), whereas numerous spherical or irregular particles, which form strips with a white contrast along the extrusion direction (ED), are present in the Mg-1.0Sn-0.7Ca and Mg-1.0Sn-0.5Zn-0.5Ca alloys (i.e. alloys III and IV, respectively). The results of energy spectrum analysis of these four alloys are listed in Table 2. From an examination of the XRD patterns (Fig. 2) in combination with the EDS results (Table 2), these few precipitates in alloys I and II are identified as the Mg_2Sn phase. According to the research of Zhao et al. [10], the Sn element in the Mg-1.0Sn and Mg-2.0Sn alloys (wt%) was present in the form of solid-solution atoms. According to the Mg-Zn phase diagram, the solid solubility of the Zn element in pure Mg at 503 K was approximately 2.5 wt% (> 0.5 wt%). Further, the electronegativity values of the Mg, Zn, and Sn elements were 1.31, 1.65, and 1.96, respectively. It is notable that the electronegativity difference between the Mg and Sn elements is larger than that between the Zn and Sn elements, which means that the Sn element preferentially reacts with the Mg element rather than with the Zn element. Therefore, the large solid solubilities of the Sn and Zn elements in Mg alloys and the relatively large electronegativity difference between the Mg and Sn elements jointly led to few Mg_2Sn phase in alloys I and II. The coarse and blocky secondary-phase particles in alloys III and IV are confirmed to be the CaMgSn phase from the EDS results and XRD patterns. Coincidentally, previous investigations [25,26] also reported that Ca addition to Mg-5Sn alloy facilitated the formation of a more thermally stable CaMgSn phase rather than the Mg_2Sn phase. It was also reported that the Sn/Ca mass ratio strongly affected the phase composition of Mg-Sn-Ca alloys. A mass ratio of 3:1 resulted in the binding of nearly all the Ca to form the CaMgSn phase, whereas an additional Mg_2Ca phase was formed at grain boundaries when the mass ratios were lower than about 2.5:1 [27]. In the present study, both the Mg-1.0Sn-0.7Ca alloy and the Mg-1.0Sn-0.5Ca-0.5Zn alloy had Sn/Ca mass ratios lower than 2.5:1. Therefore, in addition to the CaMgSn phase, the Mg_2Ca phase might have also been formed in these alloys. To further reveal the detailed of secondary phase particles formed in alloys III and IV, TEM is adopted and the

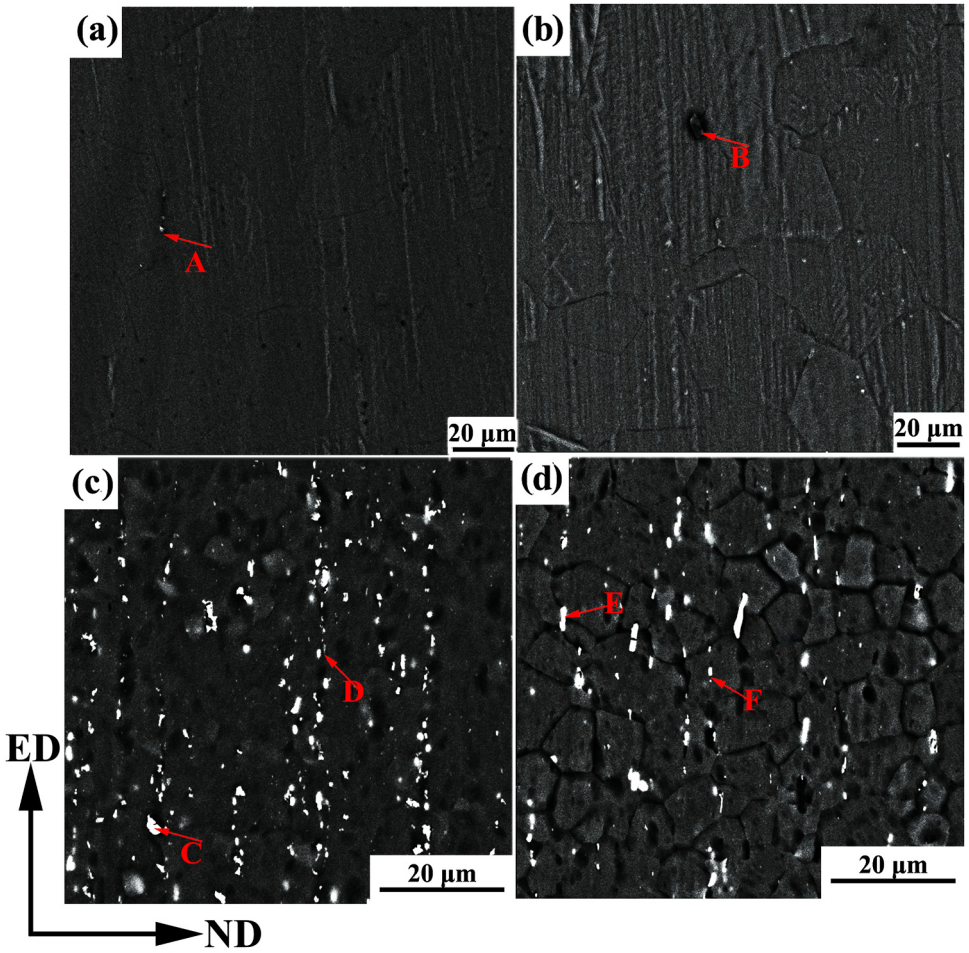

Fig. 1. Backscattered electron (BSE) SEM micrographs of as-extruded Mg-1.0Sn-based alloys: (a) Mg-1.0Sn alloy, (b) Mg-1.0Sn-0.5Zn alloy, (c) Mg-1.0Sn-0.7Ca alloy, and (d) Mg-1.0Sn-0.5Zn-0.5Ca alloy.

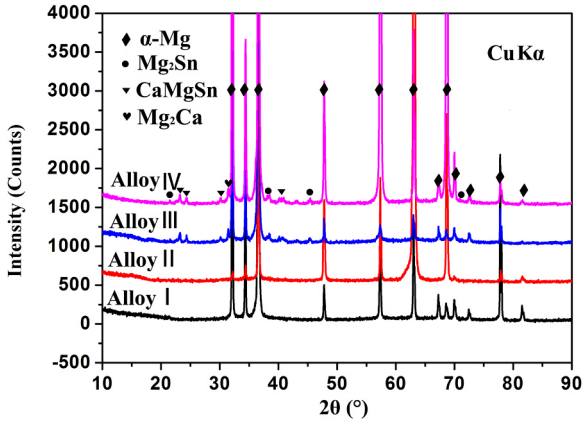

Fig. 2. XRD patterns of as-extruded Mg-1.0Sn-based alloys.

corresponding results are depicted in Fig. 3. It is observed that both alloys III and IV composed of coarse and blocky CaMgSn (sparse distribution; 475 nm–2.47 μm in length; 295–837 nm in width) along with fine and spherical Mg_2Ca (homogenous distribution; 25–101 nm in diameter) phase particles. With more details, both the volume fraction and particle size of CaMgSn phase particles in alloy III are smaller than those in corresponding alloy IV, whereas the volume fraction of Mg_2Ca phase in alloy III is more.

In order to analyse the microstructure and textural characteristics of the four as-extruded Mg-1.0Sn-based alloys, their EBSD inverse pole figure maps, (0002) pole figures, and corresponding misorientation angle distribution maps are drawn, as showed in Fig. 4. The average grain size of the Mg-1.0Sn-0.5Zn alloy (24.6 μm) is only marginally lower than that of the Mg-1.0Sn binary alloy (26.1 μm). With regard to the Ca-modified samples, obvious grain refinement exists in alloy III (9.7 μm) and alloy IV (7.2 μm). Investigation of the textural characteristics reveals that the Mg-1.0Sn and Mg-1.0Sn-0.5Zn alloys both show typical basal textures, whereas the Mg-1.0Sn-0.7Ca and Mg-1.0Sn-0.5Zn-0.5Ca alloys represent ED-tilted double-peaked textures, in which the maximum basal poles are spread ~ ± 35° from the normal direction (ND) towards the ED. Moreover, the maximum texture intensity shows a decreasing trend from alloy I to alloy IV. The misorientation angle distribution maps imply that a peak at 30° is observed for all the alloy samples. The orientation rotation of 30° around the c-axis is probably related to the processes of recrystallisation and grain

Table 2
EDS results of as-extruded Mg-1.0Sn-based alloys measured at positions marked in Fig. 1 (at%).

Position	Elements			
	Mg	Sn	Zn	Ca
A	99.6	0.4	–	–
B	99.4	0.3	0.3	–
C	75.1	15.1	–	9.8
D	94.7	4.1	–	1.2
E	87.7	6.3	0.8	5.2
F	96.2	2.7	–	1.1

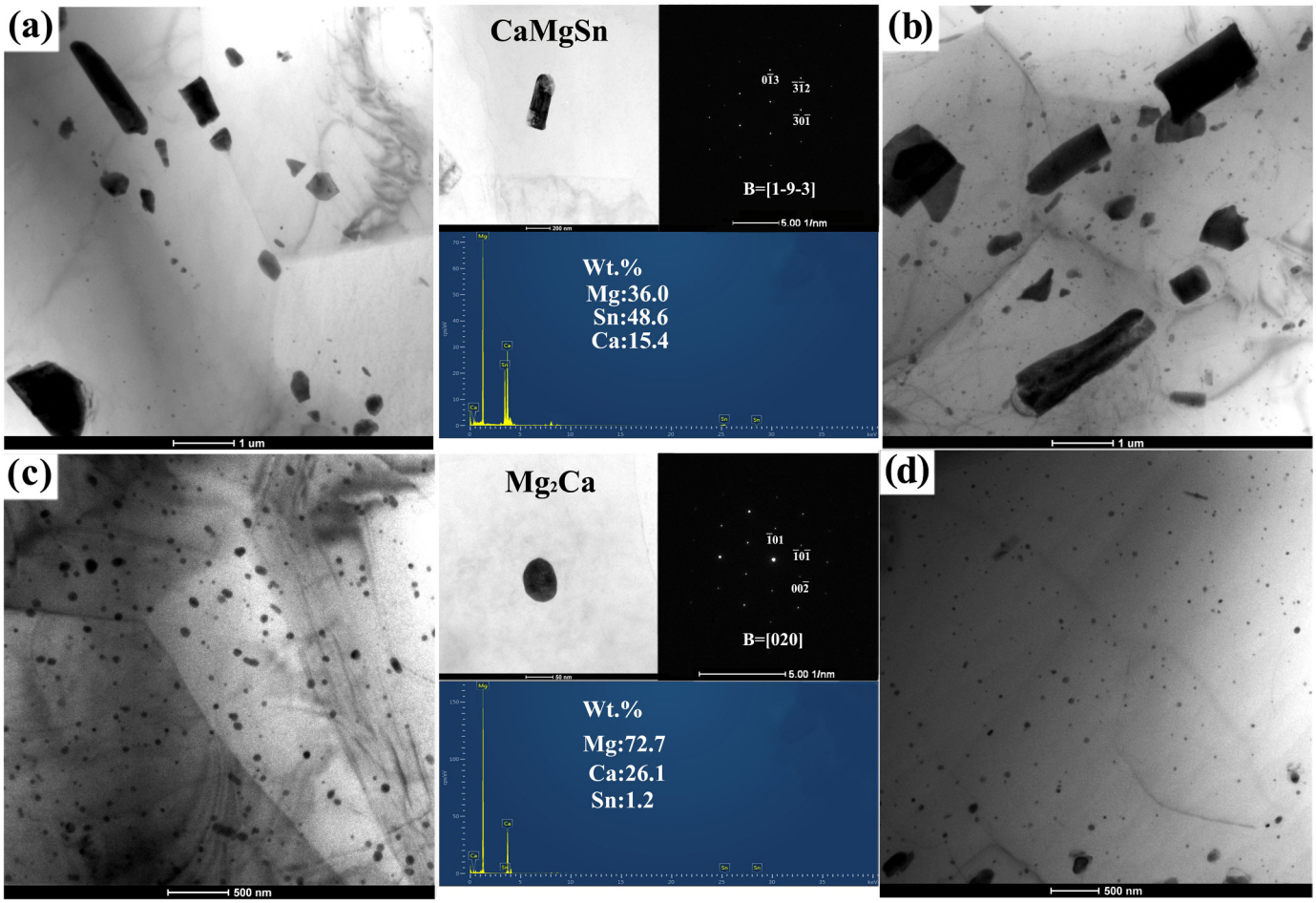

Fig. 3. Typical precipitates along with their diffraction patterns by SAED and compositions by EDS in as-extruded alloy sheets: (a, c) Mg-1.0Sn-0.5Ca alloy sheet; (b, d) Mg-1.0Sn-0.5Zn-0.5Ca alloy sheet.

growth. Biswas et al. [28] also reported that grains grew preferentially in the case of nuclei rotated by ~30° around the c-axis during the annealing process of Mg alloys. It is noteworthy that an additional peak at 60° is found only in the Ca-containing alloys. Coincidently, Wang et al. [29] revealed that a misorientation angle peak at 60° originated from the ED-split texture, wherein the c-axis of some grains may have tilted ~ ± 30° from the ND towards to the ED.

3.2. Mechanical properties

Fig. 5a and b show the true tensile stress–strain curves of the four as-extruded alloys along the ED and TD, respectively. Table 3 correspondingly lists the average values of 0.2% proof (yield) strength (YS), UTS, and EL extracted from these curves. As is observed in Fig. 5a, the YS first increases and then decreases from alloy I to alloy IV. Alloy III possesses the highest YS (137.8 MPa) among all the studied Mg-1.0Sn-based alloys; this value is about 34 MPa higher than that of alloy I. In contrast, both the UTS and the EL increase monotonously from alloy I to alloy IV. The UTS values of alloys II–IV increase by 19.3%, 21.1%, and 42.6%, respectively, compared to that of alloy I. Correspondingly, the ELs of alloys II–IV increase by 36.4%, 34.1%, and 136%, respectively, compared to that of alloy I. In addition, there are evident differences in the stress–strain responses of the alloys during the tensile tests along the ED and TD. The ductility improvement of the Mg-1.0Sn alloy via individual additions of Zn and Ca and their combined addition is relatively smaller along the TD than that along the ED. However, the increase in the YS from alloy I to alloy IV is more pronounced along the TD. In particular, the YS of alloy III attains a maximum of 209.3 MPa, which is about 73 MPa higher than that of alloy I, in tension along the TD. Strain hardening rate ($\theta = \partial\sigma/\partial\varepsilon$) versus true stress after yielding of as-extruded alloy I to alloy IV in tensile tests along the ED and TD are also represented in Fig. 5, where σ and ε are the true stress and true strain, separately. Although the tensile strain hardening rate of all alloys demonstrates a decrease with increasing stress, there are still several points worth noting. 1) θ_{III0} (hardening limit extrapolated to $\sigma = 0$) in stage III (hardening rate decreases linearly with the stress) of Ca-containing samples is much inferior to the counterpart of Ca-free samples, irrespective of tensile direction. 2) In comparison to alloys I and II, an extended and distinct stage II (an almost constant hardening behaviour) exists in Ca modified samples (alloy III and alloy IV) in tension along the ED. 3) High hardening capability in Mg-1.0Sn-0.5Zn-0.5Ca alloy in tension along the ED can greatly strengthen tensile mechanical stability, therefore obviously improving the ductility in comparison with the other samples [30].

Fig. 6 shows the secondary electron SEM fractographs of the four as-extruded Mg-1.0Sn-based alloys after tensile tests along the ED. The fracture morphology of alloy I is composed mainly of cleavage facets, whereas that of alloy II is composed of both cleavage facets and dimples. Furthermore, both alloys III and IV contain numerous fine-scale deep dimples. These different fracture surfaces of the four alloys indicate a change in the tensile fracture mode from quasi-cleavage transgranular fracture in alloys I and II to ductile fracture in alloys III and IV. Additionally, secondary-phase particles (marked by red rectangles) are detected on the fracture surfaces of both alloys III and IV As a result, it is confirmed that individual additions of minor amounts of Zn and Ca and their combined addition cause significant changes in the tensile fracture surface of the as-extruded Mg-1.0Sn alloy and that these changes are consistent with the enhancement of its ductile performance.

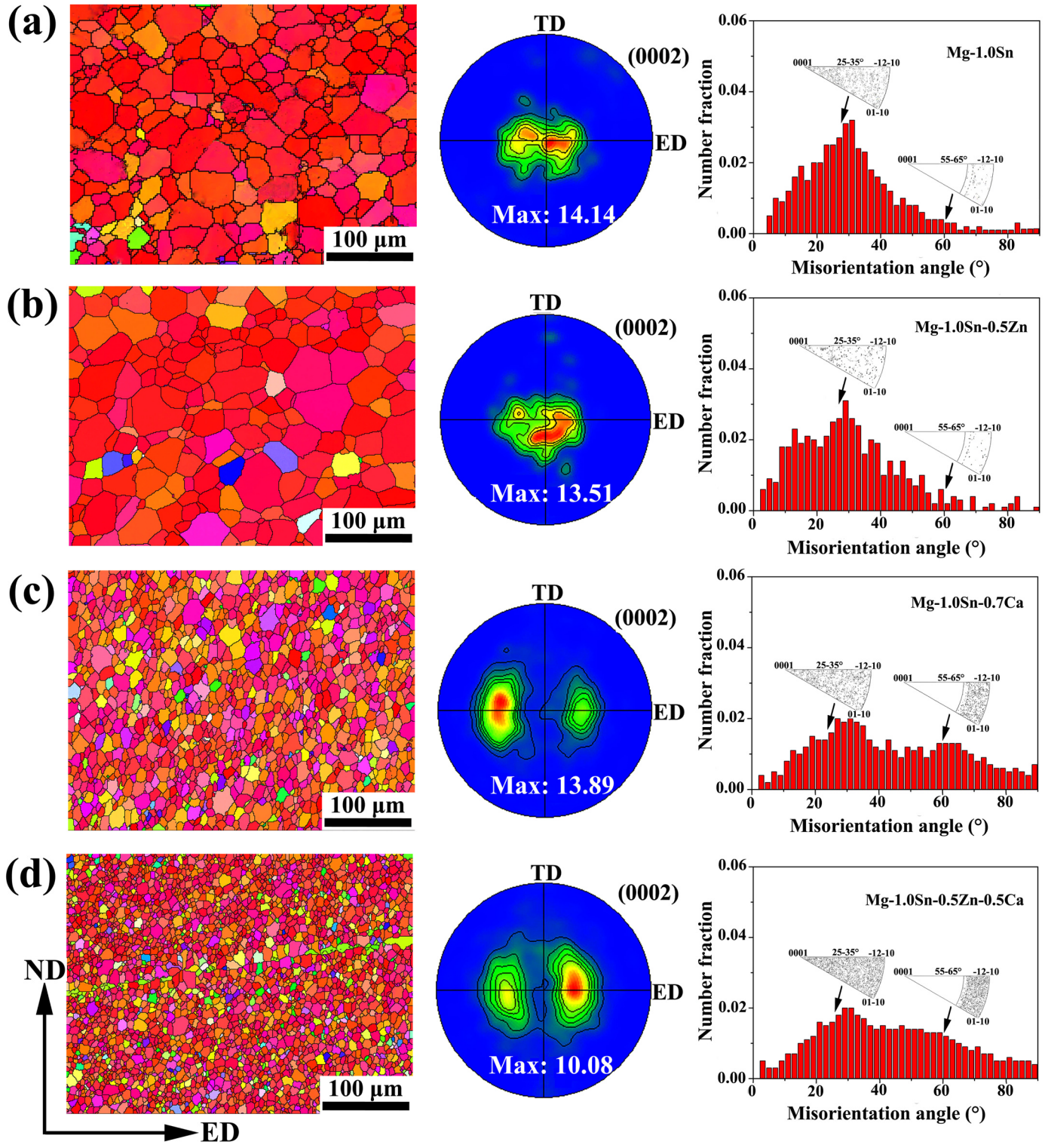

Fig. 4. EBSD inverse pole figure maps, (0002) pole figures, and misorientation angle distribution maps of four as-extruded Mg-1.0Sn-based alloys: (a) Mg-1.0Sn alloy, (b) Mg-1.0Sn-0.5Zn alloy, (c) Mg-1.0Sn-0.7Ca alloy, and (d) Mg-1.0Sn-0.5Zn-0.5Ca alloy.

4. Discussion

4.1. The microstructure variation

As showed in Fig. 4, the average grain size of alloy II is approximately 24.6 μm, which is only slightly less than that of alloy I (26.1 μm). Chen et al. [31] reported that the grain size of an as-extruded Mg-3Sn-1Al alloy decreased gradually with an increase in Zn content. The reason for this trend was that Zn-rich areas accelerated the precipitation of the Mg_2Sn phase, and these precipitates eventually hindered grain growth. In comparison, the merely slight grain refinement observed in alloy II is associated with its relatively insufficient Sn and Zn contents. With regard to the Ca-modified samples, obvious grain refinement is observed in alloy III (9.7 μm) and alloy IV (7.2 μm). This grain refinement is attributed mainly to the restraining effect from the precipitates of the thermally stable CaMgSn and Mg_2Ca phase on the

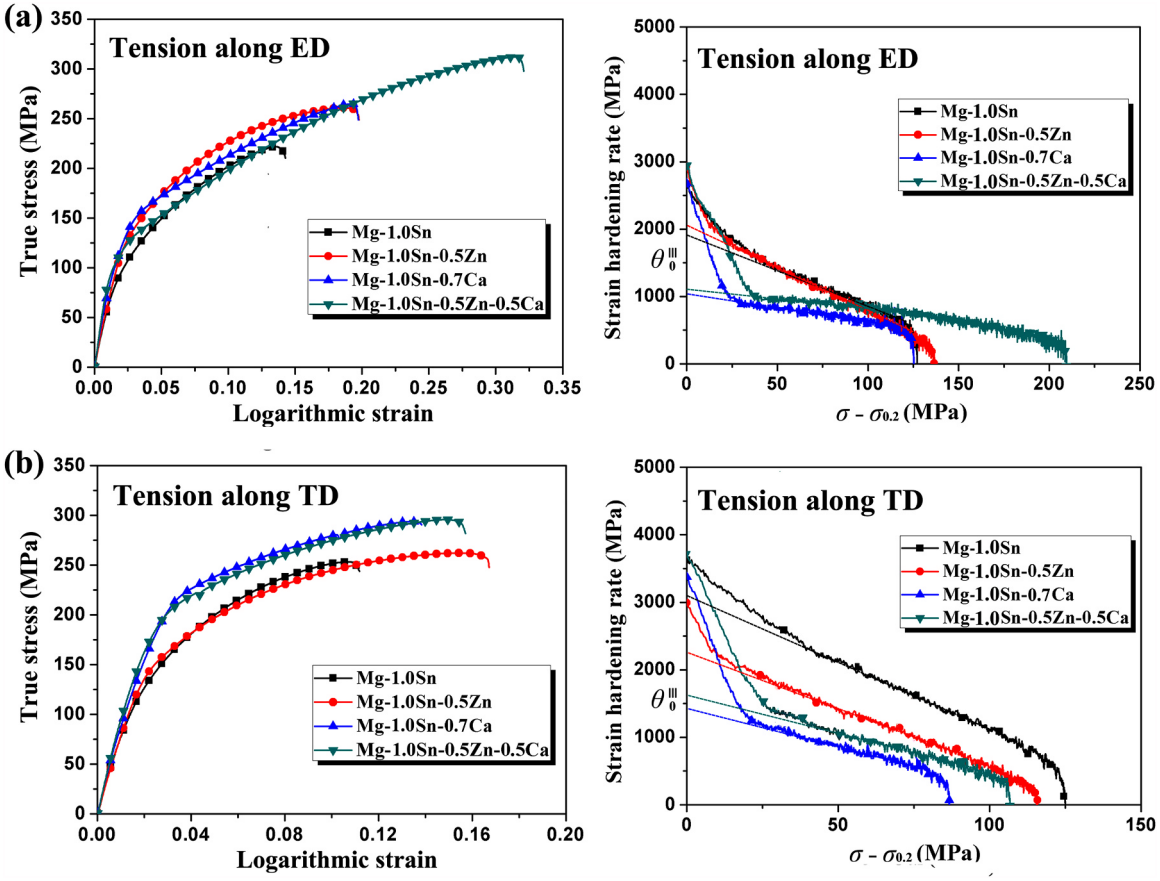

Fig. 5. True tensile stress–strain curves and strain hardening rate curves of as-extruded Mg-1.0Sn-based alloys along ED and TD. (a) Tension along ED. (b) Tension along TD.

growth of dynamically recrystallised (DRXed) grains during the extrusion process [32]. More intuitively, grains near the secondary particles are much finer than those in the region without any particles (see Fig. 1). Besides, Ca atoms can easily to segregate at grain boundaries [33], and the segregated Ca atoms may impose a strong drag force on the recrystallised grain boundaries and consequently suppress the growth of DRXed grains. However, it is worth mentioning that the average size of alloy IV is finer than that of alloy III, irrespective of the lower Ca content. The possible reason of the above phenomenon may be related with the following factors: Oh-ishi et al. [34] stated that Zn and Ca, with low mix entropy, were prone to form Ca–Zn clusters during hot extrusion. Subsequently, these Ca-Zn clusters could serve as nucleation of precipitates during extrusion or subsequent cooling [35]. Hence, it may compensate the inadequate Ca content in alloy IV to some extent. Besides, according to the research conducted by Zeng et al. [33], the co-segregation of both Zn and Ca atoms was expected to result in greater reduction of grain boundary energy than the individual segregation of Zn or Ca atoms, marking the grain boundary much less mobile. In addition, the co-segregated Zn and Ca atoms might have a larger dragging effect, than Zn or Ca atoms, of the boundary. As a result, compared with the alloy III, the finer grain structure exists in alloy IV may be associated with Ca-Zn cluster (provide more nucleation sites for precipitates) and co-segregated Zn and Ca atoms at grain boundaries (the stronger dragging effect).

Compared with alloys I and II (basal textures), the formation of weakened ED-split textures in Ca-modified alloys is associated with the solid solubility of Ca element and the particle-stimulated nucleation of recrystallisation (PSN). On the one hand, previous study [36] reported that the texture weakening of Ca-containing alloys was related to the large atomic radius and slow diffusion rate of Ca. Ding et al. [37] also revealed that the addition of solute Ca contribute to the formation of the ED-split texture in Mg alloys via reductions in the c/a ratio and stacking fault energy. On the other hand, Jiang et al. [38] reported that DRXed grains via PSN were germane to the weakening of overall texture by making the orientation coherency with parent grains diminished rapidly. The suppression or promotion effect of particles on the dynamic recrystallisation (DRX) nucleation is strongly dependent on their size; particles larger than 1 μm in size can act as effective

Table 3
Mechanical properties of four as-extruded Mg-1.0Sn based alloys.

Alloy	Tension along ED			Tension along TD		
	YS (MPa)	UTS (MPa)	EL (%)	YS (MPa)	UTS (MPa)	EL (%)
Mg-1.0Sn	103.9 ± 2.5	218.7 ± 2.9	12.9 ± 0.5	136.3 ± 2.3	253.2 ± 2.3	8.9 ± 0.3
Mg-1.0Sn-0.5Zn	129.4 ± 2.4	260.9 ± 2.7	17.6 ± 0.9	153.1 ± 1.2	262.1 ± 1.9	14.3 ± 0.6
Mg-1.0Sn-0.7Ca	137.8 ± 3.2	264.8 ± 3.2	17.3 ± 1.1	209.3 ± 3.5	293.7 ± 3.2	10.3 ± 0.5
Mg-1.0Sn-0.5Zn-0.5Ca	104.2 ± 1.8	311.9 ± 2.4	30.5 ± 1.4	188.9 ± 2.5	295.6 ± 3.4	12.9 ± 0.4

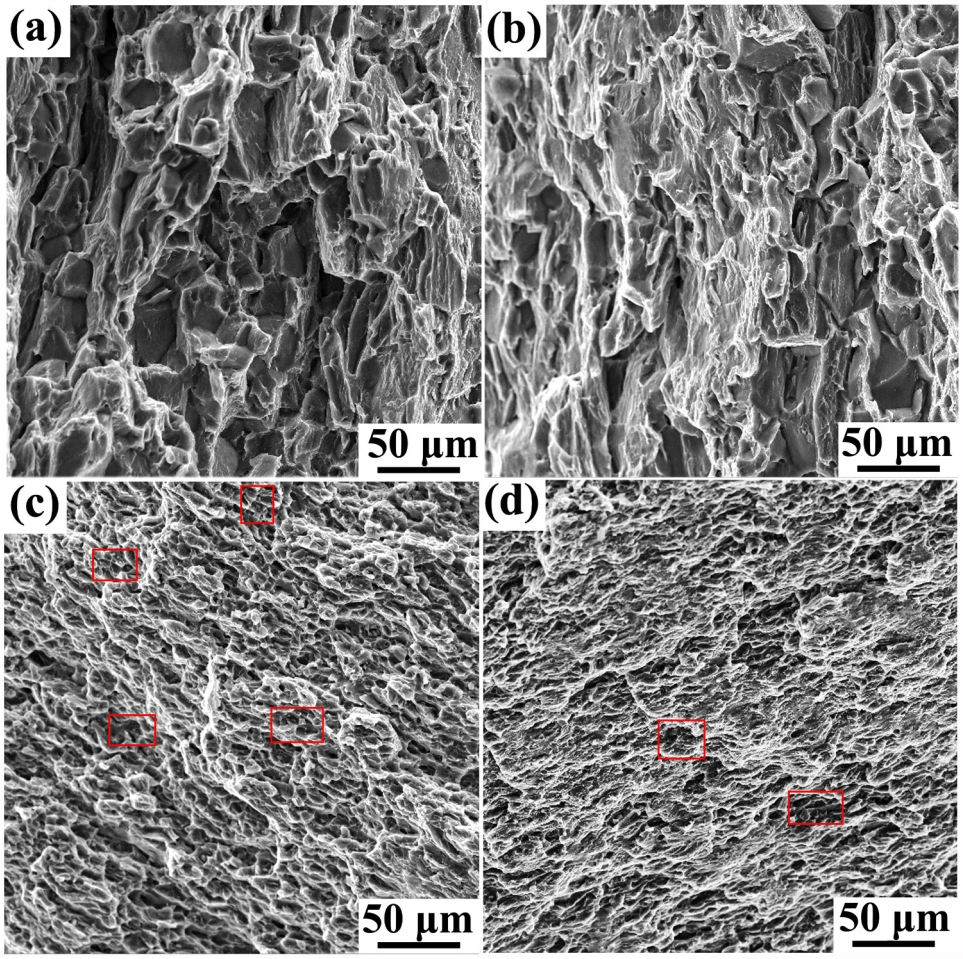

Fig. 6. Secondary electron SEM fractographs showing tensile fracture surfaces of (a) Mg-1.0Sn alloy, (b) Mg-1.0Sn-0.5Zn alloy, (c) Mg-1.0Sn-0.7Ca alloy, and (d) Mg-1.0Sn-0.5Zn-0.5Ca alloy, where the angle between the tensile direction and the ED is 0°.

nucleation sites to accelerate DRX, and vice versa [39]. Hence, the weakened textures of the Ca-containing alloys are also a result of the PSN mechanism induced by the thermally stable CaMgSn phase (> 1 μm). Besides, it is noteworthy that the addition of 0.5 wt% Zn to alloy III results in a weakened texture intensity and a broader spread of basal poles towards transverse direction (TD). It is pertained to that Zn addition can facilitate the activation of prismatic slip during the extrusion process. Similarly, previous extensive studies [40,41] have indicated that the critical resolved shear stress (CRSS) for prismatic slip decreased with an increase in Zn content.

4.2. The mechanical properties variation

In the present study, addition of 0.5 wt% Zn to the Mg-1.0Sn alloy can give rise to an improvement in both its yield strength and its ductility. Blake et al. [42] reported the occurrence of both solid-solution hardening and solid-solution softening in Mg-Zn alloys. In greater detail, solid-solution hardening caused an improvement in the yield strength on account of the tangled interaction between solute atoms and dislocations, whereas Zn solute addition induced solid-solution softening, which, in turn, resulted in an improvement in ductility via the activation of non-basal slip systems. This indicates that both solid-solution hardening and solid-solution softening contribute to the mechanical properties of Mg-Sn-Zn alloy. The enhancement of strengths of Ca-modified samples (i.e. Mg-1.0Sn-0.7Ca and Mg-1.0Sn-0.5Zn-0.5Ca alloys) compared to that of the Mg-1.0Sn binary alloy can be explained by the synergistic effects of grain refinement and precipitation strengthening. The relationship between grain size and mechanical properties is described by the Hall–Petch equation, whereas the yield strength depends on the grain size as follows:

$$\sigma_y = \sigma_0 + kd^{-1/2} \quad (1)$$

where σ_y is the yield strength, d is the average grain size, σ_0 is the friction stress for dislocation movement, and k is the Hall–Petch coefficient of Mg alloys (k = 230 MPa μm$^{1/2}$ [43]). Evidently, a reduction in grain size leads to an improvement in the yield strength. From the measured average grain sizes of alloys I, III, and IV (26.1 μm, 9.7 μm, and 7.2 μm, respectively), the increases in the yield strengths of the Mg-Sn-Ca and Mg-Sn-Zn-Ca alloys compared to that of the Mg-Sn alloy are calculated to be 37 MPa and 53 MPa, respectively. The other crucial parameter—secondary phase—also strongly affects the yield strength of Mg alloys. In general, the effect of the secondary phase on the strength is rather complex, where its morphology, size and distribution all influence the strength [44]. It is widely accepted that for precipitation strengthening, the spacing between particles should be less than several hundred nm and at the same time, the smaller the secondary phase particles size, the larger the strengthening effect. Reviewing the secondary phase particles formed in the present as-extruded Ca-modified samples (see Fig. 3), it can be deduced that sparse distributed, coarse and blocky CaMgSn phase particle cannot contribute to the high strengths of alloys effectively, whereas the homogeneous distributed, fine and granular Mg_2Ca phase may induce precipitation strengthening via block dislocation movement. Furthermore, under the assumption that the particles of thermally stable Mg_2Ca phase are not sheared by

the dislocations, their strengthening mechanism follows the Orowan process [45], and the YS is related to the uniform diameter (D) and volume fraction (f) of the secondary phase precipitates according to following equation:

$$YS \propto f^{1/2} D^{-1} \ln D \quad (2)$$

Apparently, an increase in the volume fraction of the secondary phase can lead to an improvement in the yield strength of alloys. As a result, owing to the larger amount of nano-sized Mg_2Ca phase particles formed in the Mg-1.0Sn-0.7Ca alloy, its yield strength is higher than that of the Mg-1.0Sn-0.5Zn-0.5Ca alloy, regardless of the tensile direction. Moreover, the effect of texture on the YS should not be ignored. For the purpose of assessing this effect, the distributions of the Schmid factor (SF) for basal slip of the four as-extruded alloys in tension along the ED and TD are determined, as showed in Fig. 7a and b, respectively. In general, the SF indicates feasibility and extent of activation of a certain slip mode regarding the loading direction [46]. In the present study, a higher value of average SF implies the easier activation of basal slip and consequently the lower yield strength. As shown in Fig. 5a, although alloy IV has a small grain size and some nano-sized Mg_2Ca phase particles, its yield point (104.2 MPa) is nearly identical to that of alloy I (103.9 MPa) in tension along the ED. Correspondingly, the average SF for basal slip of alloy IV (0.33) is much higher than that of alloy I (0.23), as seen in Fig. 7a. Hence, it can be deduced that the ED-split texture will offset the contributions of the fine grains and secondary phase particles to the yield strength of alloy IV in tension along the ED. Moreover, owing to the ED-split texture of the Ca-modified samples, the average SF for basal slip in tension along the ED is much higher than that along the TD and the increase in the yield strength induced by Ca addition is more pronounced in tension along the TD than along the ED.

Apparently, the Mg-1.0Sn-0.7Ca alloy exhibits higher ductility than the Mg-1.0Sn alloy in tension along the ED, because of the refined grains and weakened ED-tilted texture of the former. Moreover, it is noteworthy that a clear distinction is observed between the Mg-1.0Sn-0.7Ca alloy (alloy III) and the Mg-1.0Sn-0.5Zn-0.5Ca alloy (alloy IV) in terms of their ductile performances in tension along the ED. The EL of alloy IV is as high as 30.5%—almost double that of alloy III (17.3%). Depending on previous observations of the microstructure, it can be found that the volume fraction of coarse secondary phase particle (> 5 μm) in alloys III and IV is similar. Hence, besides the factor of secondary phase particles, the higher ductility along the ED in alloy IV compared to that of alloy III can be summarized as the following points:

1) Zn addition increases the possibility of prismatic slip activation during deformation and then contributes to accommodate strains of c-axis of grains and enhancement of uniform plastic strains. Coincidently, Hase et al. [47] also found that the alloying of Zn with Mg-Ca alloys caused a decrease in γ_{us}(prism) and then facilitated the activation of prismatic < a > slip. Fig. 8a and c display EBSD orientation maps, which showing grains and twins in alloys III and IV subjected to a strain of 0.15 along the ED. It can be found that the volume fraction of twins in alloys III (~3.85%) and IV (~4.22%) sheet is similar, which imply that twinning is not the dominant deformation mechanism to influence the ductility of sheets along the ED. To gain a better understanding of the deformation mechanisms of as-extruded alloys III and IV sheet during the tensile test, in-grain misorientation axes analysis (IGMA) is employed. Geometrically, the IGMA lying along [uvt0] could be induced by the activation of basal < a > slip and pyramidal < c+a > slip, while the IGMA lying along [0001] were by the activation of prismatic < a > slip [48]. In the present study, the IGMA in the alloy III sheet is lying mostly along < uvt0 > that are between < 10–10 > and < 2–1–10 > (see Fig. 8b), whereas the IGMA in the alloy IV is partly lying along [0001] (see Fig. 8d). Moreover, in order to intuitively prove that activation of the prismatic < a > slip can be achieved in alloy IV sheet during tensile deformation along the ED, slip traces inside the deformed grains are clearly observed. The micro stretch forming test was detailed in the report of Xia et al. [49]. As shown using the EBSD slip trace analysis method (see Fig. 8e), the traces inside grains A and B shown in the SEM images are nearly parallel to the intersection lines (red lines) between the prismatic planes of grains and the sheet plane, establishing that all can be attributed to traces of prismatic < a > slip. Based on the above results, it is verified that addition of Zn to alloy III can facilitate prismatic slip activation and consequently in favor of the high ductile performance.

2) The enhanced grain cohesion. Fig. 9 reveals the grain boundary cracks on the surface of three alloy sheets subjected to a strain of 0.1 along the ED. We can clearly observe that several intergranular cracks with smooth surfaces formed at the grain boundaries, as depicted in Fig. 9a and b, which means that the addition of Sn seems to deteriorate the stability of grain boundaries in pure Mg [50]. As for the individual Ca addition (alloy III), the length of cracks is significantly decreased, meanwhile partial cracks possess a rough surface (see Fig. 9c and d). Moreover, with Ca and Zn compound addition (alloy IV), only the lower number density grain boundary cracks form at the grain boundaries and most of them have apparently rough surface (see Fig. 9e and f). Our work is consistent with the report of Zeng et al. [22], which stated that combined additions of Zn and Ca could enhance grain boundary cohesion in the form of suppressing grain boundary cracking. In conclusion, combining the crack surface characteristic and the ductility of the as-extruded sheets suggests that individual Sn addition to pure Mg results in an embrittlement of grain boundaries. However, both individual Ca or Ca and Zn co-addition into Mg-Sn binary system can instead enhance grain boundary cohesion, leading to the high ductility, especially for the Ca-Zn co-addition.

3) The better intergranular strain propagation capacity. According to research of Cepeda-Jimenez et al. [51], the transfer of basal slip traces at the grain boundaries was largely determined by the misorientation angles of grain boundaries. With more details, it was

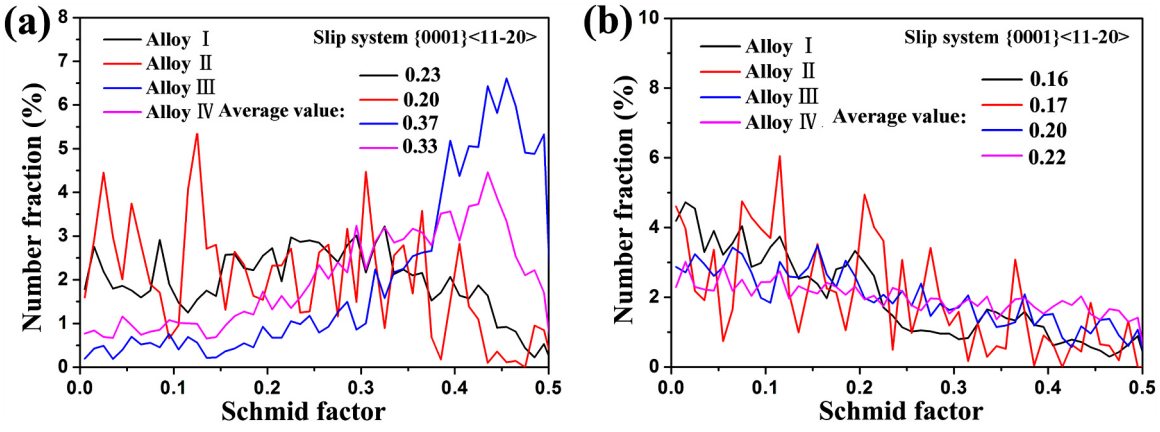

Fig. 7. Distributions of Schmid factors for basal slip systems of four as-extruded alloys in tension along (a) ED and (b) TD.

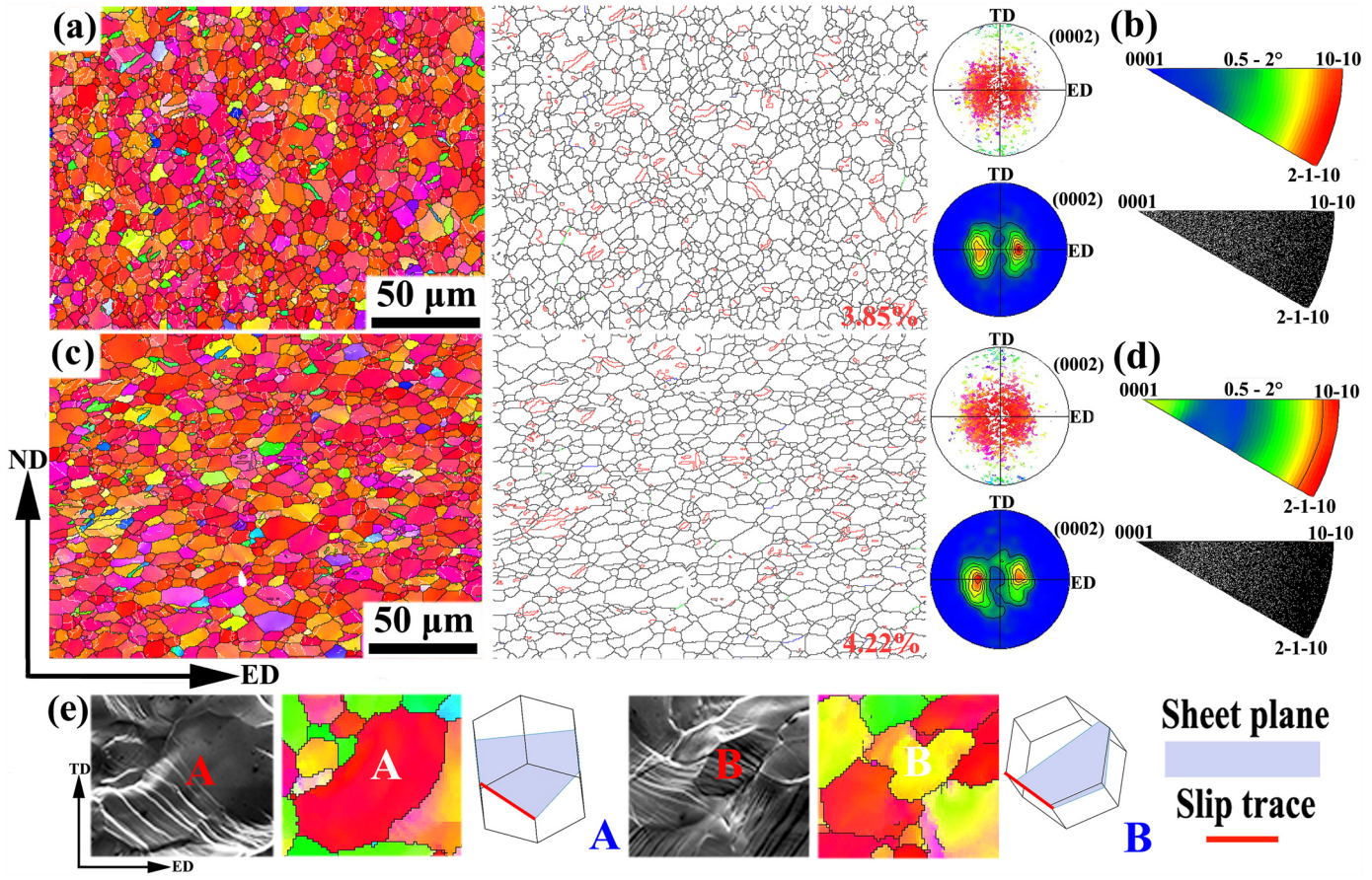

Fig. 8. EBSD orientation maps showing grains and twins in alloys III (a) and IV (c) subjected to a strain of 0.15 along the ED. IGMA analysis of the sheets subjected to tension deformation along the ED (b) the alloy III sheet. (d) the alloy IV sheet. (e) some representative examples showing prismatic slip traces in the alloy IV sheet.

difficult that basal slip traces ran through the grain boundaries with misorientation angle of beyond 35°, resulting in low ductility. Hence, the difference in ductility between alloys III and IV sheets herein may also be related to the misorientation angles of the grain boundaries. Fig. 10 shows the relationship between the slip traces and the grain boundaries in the alloys III and IV subjected to a strain of 0.1 along the ED. Obviously, as for the alloy III (see Fig. 10a and b), the slip traces within grain are not likely to run through the grain boundary between grains 4, 5, 7 and 8 with misorientation angle of 40.25–76.44°, whereas the misorientation angle between grains 1, 2 and 3 (as well as grains 4 and 5; see Fig. 10c and d) is 13.08–31.09°, slip traces appeared to transfer across grain boundaries from one grain to a neighbouring grain. Depending on EBSD data, the misorientation angles are counted in the alloys III and IV sheets before tension to a 0.1 plastic strain. The result reflects that the volume fraction about 18.9% of the misorientation angles from 15° to 35° in the alloy IV sheet is more than that about 12.5% in the alloy III sheet.

As a result, the more activated prismatic slip, the enhanced grain cohesion and the better intergranular strain propagation capacity jointly lead to the higher ductile performance in alloy IV than that of alloy III in tension along the ED.

4.3. The strain hardening behaviour variation

As shown in Fig. 5a, an almost linear decrease in the strain hardening rate is observed for the Ca-free alloys (i.e. alloys I and II), whereas a prolonged stage II (an almost constant hardening behaviour) and a delayed decrease in the strain hardening rate are observed for the Ca-modified alloys (i.e. alloys III and IV). The main reason for these trends is that different types of textures affect the dynamic recovery in different ways by inducing changes in the orientation factors for basal and prismatic slips [52]. Alloys I and II both show typical basal textures, whereas alloys III and IV show ED-split double-peaked textures. Thus, the easier activation of basal slip in the Ca-modified alloys during tensile tests along the ED may suppress the dynamic recovery induced by the cross-slip of the < a > dislocations from the basal plane to the prismatic plane and subsequently contribute to the retention of an evident stage II. Furthermore, although alloy III also shows a distinct stage II, the length of its stage II is significantly shorter than that of alloy IV. This difference is possibly attributable to the difference in the volume amount of secondary-phase particles between alloys III and IV. Luo et al. [53] also expressed that secondary-phase particles underwent severe cracking under tensile deformation, and this could further reduce the strain hardening rate because of the consequent local softening.

It is worth mentioning that the θ_{III0} (i.e. the hardening limit extrapolated to $\sigma = 0$) values of the Ca-modified samples in stage III (wherein the strain hardening rate decreases linearly with the stress) are much smaller than the corresponding values of the Ca-free samples. In general, the strain hardening rate (θ) in stage III is related to the competition between dislocation storage (accumulation) and the dynamic recovery response (annihilation). On the one hand, a fine grain size was reported to cause a decrease in the dislocation storage capacity and in the difference in the flow resistance between grain boundary and interior, which, in turn, led to a decrease in the hardening capacity [54,55]. On the other hand, during plastic deformation, dislocations were more likely to be trapped by grain boundaries, and subsequently reorganisation occurred inside the boundaries [56]. Specifically, the relaxation time (τ) for dislocations that dissociate into grain boundaries can be expressed as follows:

$$\tau = (\rho b d)/(\alpha \varepsilon) \quad (3)$$

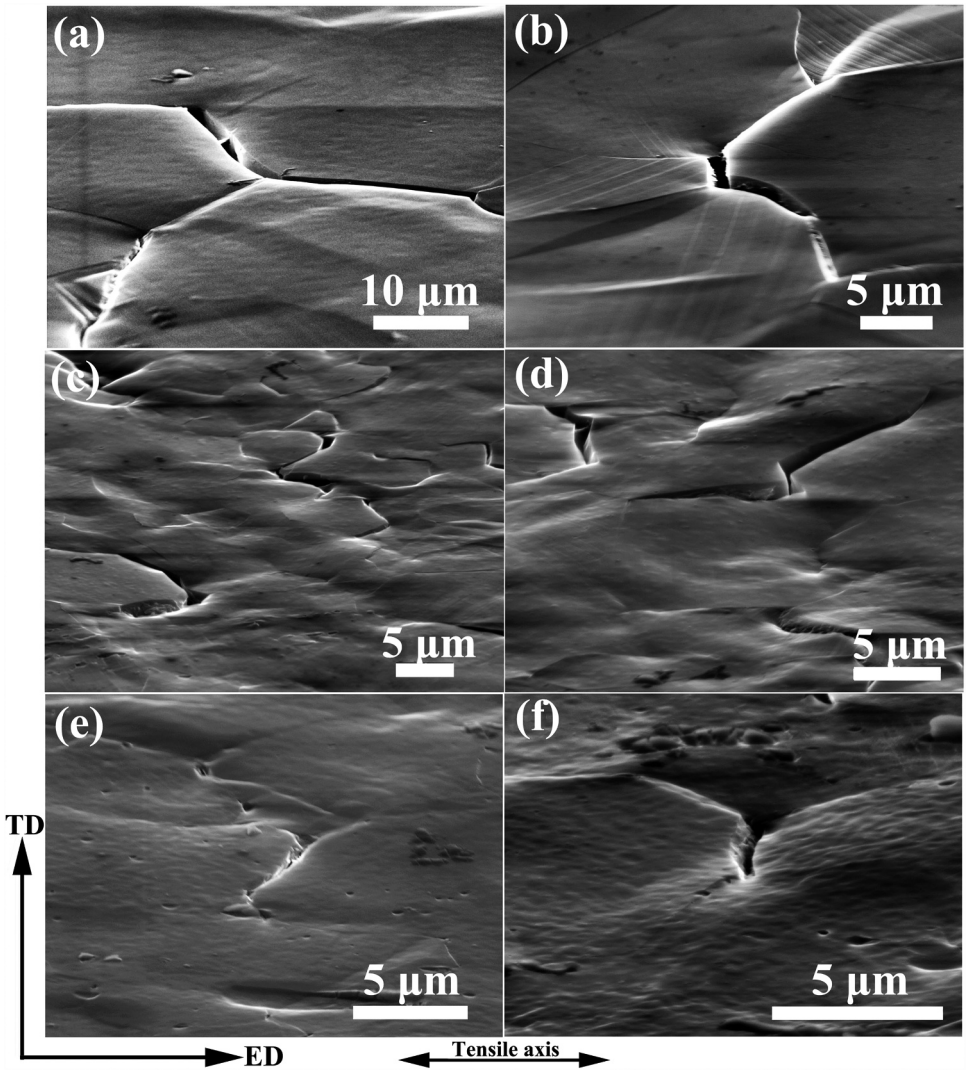

Fig. 9. Secondary electron SEM micrographs showing grain boundary cracks in the sheets subjected to a strain of 0.1 along the ED: (a, b) the Mg-1.0Sn alloy sheet; (c, d) the Mg-1.0Sn-0.5Ca alloy sheet; (e, f) the Mg-1.0Sn-0.5Zn-0.5Ca alloy sheet.

where ρ is the dislocation density, $\dot{\varepsilon}$ is the strain rate, d is the grain size, and α is a geometric term related to the contributions of active dislocations. Hence, dynamic recovery tends to accelerate as the grain size decreases, and consequently, the work hardening rate decreases. As a result, the obvious grain refinement results in a sharp decrease in θ_{II10} in the strain hardening rate curves of the Ca-modified samples than that of the Ca-free samples.

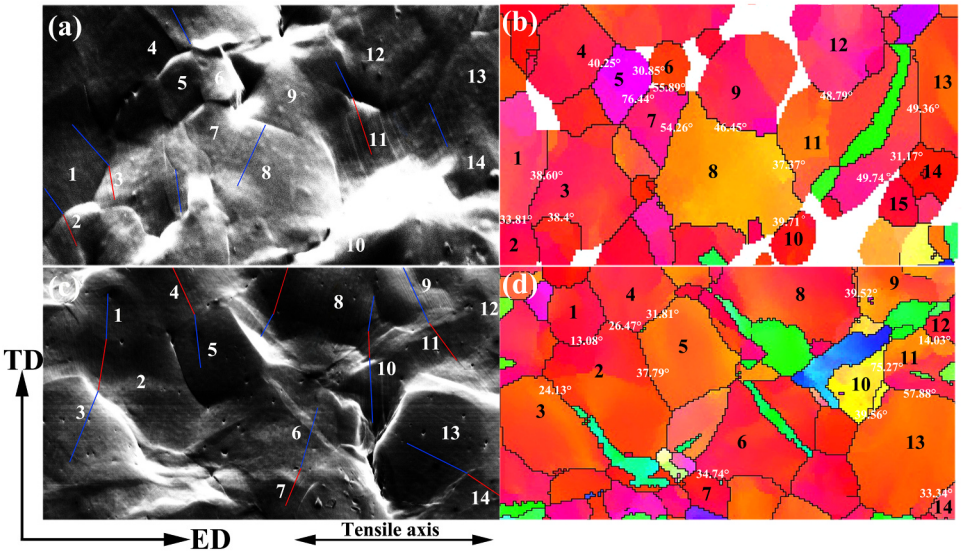

Fig. 10. Secondary electron SEM micrographs in (a) the Mg-1.0Sn-0.5Ca alloy and (c) the Mg-1.0Sn-0.5Zn-0.5Ca alloy sheets subjected to a strain of 0.1 along the ED. The misorientation angles of the grain boundaries are plotted in the corresponding EBSD IPF maps of (b) the Mg-1.0Sn-0.5Ca alloy sheet and (d) the Mg-1.0Sn-0.5Zn-0.5Ca alloy sheet.

5. Conclusions

1. Both the Mg-1.0Sn alloy and the Mg-1.0Sn-0.5Zn alloy showed relatively coarse grains and typical strong basal textures, whereas the Mg-1.0Sn-0.7Ca and Mg-1.0Sn-0.5Zn-0.5Ca alloys showed obvious grain refinement, some CaMgSn and Mg_2Ca phase particles, and weakened ED-tilted double-peaked textures.
2. The addition of 0.5 wt% Zn improved both the yield strength and the ductility of the Mg-1.0Sn alloy because of the combined effects of solid-solution hardening and solid-solution softening. The significantly increased yield strength of the Mg-1.0Sn-0.7Ca alloy compared to that of the Mg-1.0Sn alloy was a result of grain refinement and precipitation strengthening, whereas the ductility improvement of the former alloy was attributed to the refined grains and weakened ED-tilted texture. Moreover, the much better ductile performance of the Mg-1.0Sn-0.5Zn-0.5Ca alloy in tension along the ED than that of the Mg-1.0Sn-0.7Ca alloy was mainly ascribed to the increased activation of prismatic slip, enhanced of grain boundary cohesion, and improved intergranular strain propagation capacity.
3. Individual addition of Ca as well as the combined addition of Zn and Ca both strongly affected the strain hardening behaviour of the Mg-1.0Sn alloy. The evident and prolonged stage II in the strain hardening rate curves of the Ca-modified samples was associated with their ED-split textures and the resultant enhancement of basal slip activity. Moreover, the obvious grain refinement of the Ca-modified samples caused a strong decrease in the extrapolated hardening rate (θ_{III0}).

Acknowledgements

The authors are grateful for the financial supports from the Special major R & D Projects for Key Technology Innovation of Key Industries in Chongqing, China (Grant No. cstc2017zdcy-zdzxX0006), Chongqing Science and Technology Commission, China (cstc2017zdcy-zdzxX0006, cstc2017jcyjAX0012, cstc2015zdcy-ztzx50003 and cstc2015yykfc5001), National Natural Science Foundation of China, China (51531002 and U1764253), and the National Key Research and Development Program of China, China (2016YFB0301104 and 2016YFB0101700), Chongqing Scientific & Technological Talents Program, China (KJXX2017002), China Postdoctoral Science Foundation, China (2018T110948).

References

[1] X.B. Zheng, W.B. Du, K. Liu, Z.H. Wang, S.B. Li, Effect of trace addition of al on microstructure, texture and tensile ductility of Mg-6Zn-0.5Er alloy, J. Magnes. Alloy. 4 (2016) 135–139.
[2] J. Xu, J.F. Song, B. Jiang, J.J. He, Q.H. Wang, B. Liu, G.S. Huang, F.S. Pan, Effect of effective strain gradient on texture and mechanical properties of Mg-3Al-1Zn alloy sheets produced by asymmetric extrusion, Mater. Sci. Eng. A 706 (2017) 172–180.
[3] T. Laser, C. Hartig, M.R. Nürnberg, D. Letzig, R. Bormann, The influence of calcium and cerium mischmetal on the microstructural evolution of Mg-3Al-1Zn during extrusion and resulting mechanical properties, Acta Mater. 56 (2008) 2791–2798.
[4] F.L. Guo, B. Feng, S.W. Fu, Y.C. Xin, S.W. Xu, Q. Liu, Microstructure and texture in an extruded Mg-Al-Ca-Mn flat-oval tube, J. Magnes. Alloy. 5 (2017) 13–19.
[5] T.T. Tong, F. Zhang, S.H. Liu, Y. Du, K. Li, Experimental investigation on the phase equilibria of the Mg-Sn-Ag system in the Mg-rich corner, J. Magnes. Alloy. 5 (2017) 41–47.
[6] L. Gao, R.S. Chen, E.H. Han, Effects of rare-earth elements Gd and Y on the solid solution strengthening of Mg alloys, J. Alloy. Compd. 481 (2009) 379–384.
[7] J.B. Liu, K. Zhang, J.T. Han, X.G. Li, Y.J. Li, M.L. Ma, J.W. Yuan, G.L. Shi, M. Li, C.F. Lu, Study on the microstructure and mechanical Properties of WE71 magnesium alloy, Mater. Sci. Eng. A 625 (2015) 107–113.
[8] Y. Kanazawa, M. Kamitani, Rare Earth minerals and resources in the world, J. Alloy. Compd. 408–412 (2006) 1339–1343.
[9] H.M. Liu, Y.G. Chen, Y.B. Tang, S.H. Wei, G. Niu, The microstructure, tensile properties, and creep behavior of as-cast Mg-(1-10)%Sn alloys, J. Alloy. Compd. 440 (2007) 122–126.
[10] C.Y. Zhao, X.H. Chen, F.S. Pan, S.Y. Gao, D. Zhao, X.F. Liu, Effect of Sn content on strain hardening behavior of as-extruded Mg-Sn alloys, Mater. Sci. Eng. A 713 (2018) 244–252.
[11] H.Y. Wang, N. Zhang, C. Wang, Q.C. Jiang, First-principles study of the generalized stacking fault energy in Mg-3Al-3Sn alloy, Scr. Mater. 65 (2011) 723–726.
[12] F.R. Elsayed, T.T. Sasaki, T. Ohkubo, H. Takahashi, S.W. Xu, S. Kamado, K. Hono, Effect of extrusion conditions on microstructure and mechanical properties of microalloyed Mg-Sn-Al-Zn alloys, Mater. Sci. Eng. A 588 (2013) 318–328.
[13] T.T. Sasaki, F.R. Elsayed, T. Nakata, T. Ohkubo, S. Kamado, K. Hono, Strong and ductile heat-treatable Mg-Sn-Zn-Al wrought alloys, Acta Mater. 99 (2015) 176–186.
[14] Y.F. Chai, B. Jiang, J.F. Song, Q.H. Wang, H. Gao, B. Liu, G.S. Huang, D.F. Zhang, F.S. Pan, Improvement of mechanical properties and reduction of yield asymmetry of extruded Mg-Sn-Zn alloy through Ca addition, J. Alloy. Compd. 782 (2019) 1076–1086.
[15] T.T. Sasaki, K. Yamamoto, T. Honma, S. Kamado, K. Hono, A high-strength Mg-Sn-Zn-Al alloy extruded at low temperature, Scr. Mater. 59 (2008) 1111–1114.
[16] C.Q. Liu, H.W. Chen, H. Liu, X.J. Zhao, J.F. Nie, Metastable precipitate phases in Mg-9.8 wt% Sn alloy, Acta Mater. 144 (2017).
[17] W.L. Cheng, S.S. Park, B.S. You, B.H. Koo, Microstructure and mechanical properties of binary Mg-Sn alloys subjected to indirect extrusion, Mater. Sci. Eng. A 527 (2010) 4650–4653.
[18] Y.J. Wang, J. Peng, L.P. Zhong, On the microstructure and mechanical property of as-extruded Mg-Sn-Zn alloy with Cu addition, J. Alloy. Compd. 744 (2018) 234–242.
[19] T.T. Sasaki, K. Oh-Ishi, T. Ohkubo, K. Hono, Enhanced age hardening response by the addition of Zn in Mg-Sn alloys, Scr. Mater. 55 (2006) 251–254.
[20] H.C. Pan, G.W. Qin, Y.M. Huang, Y.P. Ren, X.C. Sha, X.D. Han, Z.Q. Liu, C.F. Li, X.L. Wu, H.W. Chen, C. He, L.J. Chai, Y.Z. Wang, J.F. Nie, Development of low-alloyed and rare-earth-free magnesium alloys having ultra-high strength, Acta Mater. 149 (2018) 350–363.
[21] H.C. Pan, G.W. Qin, M. Xu, H. Fu, Y.P. Ren, F.S. Pan, Z.Y. Gao, C.Y. Zhao, Q.S. Yang, J. She, B. Song, Enhancing mechanical properties of Mg-Sn alloys by combining addition of Ca and Zn, Mater. Des. 83 (2015) 736–744.
[22] Z.R. Zeng, M.Z. Bian, S.W. Xu, C.H.J. Davies, N. Birbilis, J.F. Nie, Effects of dilute additions of Zn and Ca on ductility of magnesium alloy sheet, Mater. Sci. Eng. A 674 (2016) 459–471.
[23] Y. Chino, T. Ueda, Y. Otomatsu, K. Sassa, X.S. Huang, K. Suzuki, M. Mabuchi, Effects of Ca on tensile properties and stretch formability at room temperature in Mg-Zn and Mg-Al alloys, Mater. Trans. 52 (2011) 1477–1482.
[24] Y. Chino, K. Sassa, X.S. Huang, K. Suzuki, M. Mabuchi, Effects of zinc concentration on the stretch formability at room temperature of the rolled Mg-Zn-Ca Alloys, J. Jpn. Inst. Met. 75 (2011) 35–41.
[25] G. Nayyeri, R. Mahmudi, Effects of Ca additions on the microstructural stability and mechanical properties of Mg-5% Sn alloy, Mater. Des. 32 (2011) 1571–1576.
[26] G.H. Hasani, R. Mahmudi, Tensile properties of hot rolled Mg-3Sn-1Ca alloy sheets at elevated temperatures, Mater. Des. 32 (2011) 3736–3741.
[27] K.P. Rao, Y.V.R.K. Prasad, K. Suresh, N. Hort, K.U. Kainer, Hot deformation behavior of Mg-2Sn-2Ca alloy in as-cast condition and after homogenization, Mater. Sci. Eng. A 552 (2012) 444–450.
[28] S. Biswas, B. Beausir, L.S. Toth, S. Suwas, Evolution of texture and microstructure during hot torsion of a magnesium alloy, Acta Mater. 61 (2013) 5263–5277.
[29] G.G. Wang, G.S. Huang, X. Chen, Q.Y. Deng, A.T. Tang, B. Jiang, F.S. Pan, Effects of Zn addition on the mechanical properties and texture of extruded Mg-Zn-Ca-Ce magnesium alloy sheets, Mater. Sci. Eng. A 705 (2017) 46–54.
[30] N. Afrin, D.L. Chen, X. Cao, M. Jahazi, Strain hardening behavior of a friction stir welded magnesium alloy, Scr. Mater. 57 (2007) 1004–1007.
[31] Y.A. Chen, L. Jin, Y. Song, H. Liu, R.Y. Ye, Effect of Zn on microstructure and mechanical property of Mg-3Sn-1Al alloys, Mater. Sci. Eng. A 612 (2014) 96–101.
[32] C.Y. Zhao, F.S. Pan, H.C. Pan, Microstructure, mechanical and bio-corrosion properties of as-extruded Mg-Sn-Ca alloys, Trans. Nonferr. Met. Soc. China 26 (2016) 1574–1582.
[33] Z.R. Zeng, Y.M. Zhu, S.W. Xu, M.Z. Bian, C.H.J. Davies, N. Birbilis, J.F. Nie, Texture evolution during static recrystallization of cold-rolled magnesium alloys, Acta Mater. 105 (2016) 479–494.
[34] K. Oh-ishi, R. Watanabe, C.L. Mendis, K. Hono, Age-hardening response of Mg–0.3 at% Ca alloys with different Zn contents, Mater. Sci. Eng. A 526 (2009) 177–184.
[35] Y.Z. Du, X.G. Qiao, M.Y. Zheng, K. Wu, S.W. Xu, The microstructure, texture and mechanical properties of extruded Mg–5.3Zn–0.2Ca–0.5Ce (wt%) alloy, Mater. Sci. Eng. A 620 (2015) 164–171.
[36] N. Stanford, The effect of calcium on the texture, microstructure and mechanical properties of extruded Mg-Mn-Ca alloys, Mater. Sci. Eng. A 528 (2010) 314–322.
[37] H.L. Ding, X.B. Shi, Y.Q. Wang, G.P. Cheng, S. Kamado, Texture weakening and ductility variation of Mg-2Zn alloy with CA or RE addition, Mater. Sci. Eng. A 645 (2015) 196–204.
[38] M.G. Jiang, H. Yan, R.S. Chen, Twinning, recrystallization and texture development during multi-directional impact forging in an AZ61 Mg alloy, J. Alloy. Compd. 650 (2015) 399–409.
[39] J.D. Robson, D.T. Henry, B. Davis, Particle effects on recrystallization in magnesium–manganese alloys: particle-stimulated nucleation, Acta Mater. 57 (2009) 2739–2747.
[40] C.Y. Zhao, X.H. Chen, F.S. Pan, J.F. Wang, S.Y. Gao, T. Tu, C.Q. Liu, J.H. Yao, A. Atrens, Strain hardening of as-extruded Mg-xZn (x = 1, 2, 3 and 4 wt%) alloys, J. Mater. Sci. Technol. 35 (2019) 142–150.
[41] A. Akhtar, E. Teghtsoonian, Solid solution strengthening of magnesium single crystals—ii the effect of solute on the ease of prismatic slip, Acta Metal. 17 (1969) 1351–1356.
[42] A.H. Blake, C.H. Cáceres, Solid-solution hardening and softening in Mg–Zn alloys, Mater. Sci. Eng. A 483–484 (2008) 161–163.
[43] H.H. Yu, C.Z. Li, Y.C. Xin, A. Chapuis, X.X. Huang, Q. Liu, The mechanism for the high dependence of the Hall-Petch slope for twinning/slip on texture in Mg alloys, Acta Mater. 128 (2017) 313–326.

[44] Y.F. Chai, B. Jiang, J.F. Song, Q.H. Wang, J.J. He, J. Zhao, G.S. Huang, Z.T. Jiang, F.S. Pan, Role of Al content on the microstructure, texture and mechanical properties of Mg-3.5Ca based alloys, Mater. Sci. Eng. A 730 (2018) 303–316.
[45] J.F. Nie, Effects of precipitate shape and orientation on dispersion strengthening in magnesium alloys, Scr. Mater. 48 (2003) 1009–1015.
[46] Q.H. Wang, B. Jiang, A.T. Tang, S.X. Ma, Z.T. Jiang, Y.F. Chai, B. Liu, F.S. Pan, Ameliorating the mechanical properties of magnesium alloy: role of texture, Mater. Sci. Eng. A 689 (2017) 395–403.
[47] T. Hase, T. Ohtagaki, M. Yamaguchi, N. Ikeo, T. Mukai, Effect of aluminum or zinc solute addition on enhancing impact fracture toughness in Mg–Ca alloys, Acta Mater. 104 (2016) 283–294.
[48] J.P. Hadorn, K. Hantzsche, S. Yi, J. Bohlen, D. Letzig, J.A. Wollmershauser, S.R. Agnew, Role of solute in the texture modification during hot deformation of Mg-Rare earth alloys, Metall. Mater. Trans. A 43 (2012) 1347–1362.
[49] D.B. Xia, G.S. Huang, Q.Y. Deng, B. Jiang, S.S. Liu, F.S. Pan, Influence of stress state on microstructure evolution of AZ31 Mg alloy rolled sheet during deformation at room temperature, Mater. Sci. Eng. A 715 (2018) 379–388.
[50] Q.H. Wang, Y.Q. Shen, B. Jiang, A.T. Tang, J.F. Song, Z.T. Jiang, T.H. Yang, G.S. Huang, F.S. Pan, A micro-alloyed Mg-Sn-Y alloy with high ductility at room temperature, Mater. Sci. Eng. A 735 (2018) 131–144.
[51] C.M. Cepeda-Jimenez, J.M. Molina-Aldareguia, M.T. Perez-Prado, Effect of grain size on slip activity in pure magnesium polycrystals, Acta Mater. 84 (2015) 443–456.
[52] J.A.D. Valle, F. Carreño, O.A. Ruano, Influence of texture and grain size on work hardening and ductility in magnesium-based alloys processed by ECAP and rolling, Acta Mater. 54 (2006) 4247–4259.
[53] J. Luo, H. Yan, N. Zheng, R.S. Chen, Effects of zinc and calcium concentration on the microstructure and mechanical properties of hot-rolled Mg-Zn-Ca sheets, Acta Metal. Sin. (Engl. Lett.) 29 (2016) 205–216.
[54] J. Luo, Z. Mei, W.H. Tian, Z.R. Wang, Diminishing of work hardening in electroformed polycrystalline copper with nano-sized and uf-sized twins, Mater. Sci. Eng. A 441 (2006) 282–290.
[55] S.M. Chowdhury, D.L. Chen, S.D. Bhole, X. Cao, E. Powidajko, D.C. Weckman, Y. Zhou, Tensile properties and strain-hardening behavior of double-sided arc welded and friction stir welded AZ31B magnesium alloy, Mater. Sci. Eng. A 527 (2010) 2951–2961.
[56] E. Ma, Y.M. Wang, Q.H. Lu, M.L. Sui, L. Lu, K. Lu, Strain hardening and large tensile elongation in ultrahigh-strength nano-twinned copper, Appl. Phys. Lett. 85 (2004) 4932–4934.